This Accepted Manuscript has not been copyedited and formatted. The final version may differ from this version.

JNeurosci
THE JOURNAL OF NEUROSCIENCE

Research Articles: Systems/Circuits

Pathway specific drive of cerebellar Golgi cells reveals integrative rules of cortical inhibition

Sawako Tabuchi[1], Jesse I. Gilmer[1,2], Karen Purba[1] and Abigail L. Person[1]

[1]*Department of Physiology & Biophysics*

[2]*Neuroscience Graduate Program, University of Colorado Denver, University of Colorado School of Medicine Aurora, CO 80045*

https://doi.org/10.1523/JNEUROSCI.1448-18.2018

Received: 7 June 2018

Revised: 27 November 2018

Accepted: 13 December 2018

Published: 26 December 2018

Author contributions: S.T., J.I.G., and A.L.P. designed research; S.T., J.I.G., and A.L.P. performed research; S.T., J.I.G., K.P., and A.L.P. analyzed data; S.T. wrote the first draft of the paper; S.T., J.I.G., and A.L.P. edited the paper; S.T. wrote the paper.

Conflict of Interest: The authors declare no competing financial interests.

We thank Ms Samantha Lewis for expert technical support during the project and Dr. Christian Rickert for assistance with dynamic clamp design. This work was supported by the Japan Society for The Promotion of Science (JSPS) Overseas Research Fellowship and The Uehara Memorial Foundation research fellowship to ST; and the Klingenstein Foundation, the Boettcher Foundation Webb-Waring biomedical research award and NS084996 to ALP and the Neuroscience Training Grant (T32NS 099042 to JIG). Imaging experiments were performed in the University of Colorado Anschutz Medical Campus Advance Light Microscopy Core supported in part by Rocky Mountain Neurological Disorders Core Grant Number P30NS048154 and by NIH/ NCATS Colorado CTSI Grant Number UL1 TR001082. Engineering support was provided by the Optogenetics and Neural Engineering Core at the University of Colorado Anschutz Medical Campus, funded in part by the National Institute of Neurological Disorders and Stroke of the National Institutes of Health under award number P30NS048154.

Address for Correspondence: Abigail L. Person, Ph.D., Department of Physiology & Biophysics, University of Colorado School of Medicine, 12800 East 19th Ave, RC-1 North, Campus Box 8307, Aurora, CO 80045, USA, email: abigail.person@ucdenver.edu, (303) 724-4514

Cite as: J. Neurosci 2018; 10.1523/JNEUROSCI.1448-18.2018

Alerts: Sign up at www.jneurosci.org/alerts to receive customized email alerts when the fully formatted version of this article is published.

Accepted manuscripts are peer-reviewed but have not been through the copyediting, formatting, or proofreading process.

Copyright © 2018 the authors

JNeurosci Accepted Manuscript

JNeurosci Accepted Manuscript

1
2 **Pathway specific drive of cerebellar Golgi cells reveals integrative rules of cortical**
3 **inhibition**
4
5 *Sawako Tabuchi[1], Jesse I. Gilmer[1,2], Karen Purba[1], Abigail L. Person[1]*
6 *1. Department of Physiology & Biophysics*
7 *2. Neuroscience Graduate Program, University of Colorado Denver*
8 *University of Colorado School of Medicine Aurora, CO 80045*
9
10 **Abstract: 229 words**
11 **Significance Statement: 109**
12 **Introduction: 514**
13 **Discussion: 1,574 words**
14 **Figures: 6**
15 **Tables: 0**
16 **Abbreviated title: Golgi cell structure-function relationship**
17
18 **Address for Correspondence:**
19 Abigail L. Person, Ph.D.
20 Department of Physiology & Biophysics
21 University of Colorado School of Medicine
22 12800 East 19th Ave
23 RC-1 North
24 Campus Box 8307
25 Aurora, CO 80045
26 USA
27 email: abigail.person@ucdenver.edu
28 (303) 724-4514
29
30 **Conflict of Interest:** The authors declare no competing financial interests.
31
32 **Acknowledgements:** We thank Ms Samantha Lewis for expert technical support during the
33 project and Dr. Christian Rickert for assistance with dynamic clamp design. This work was
34 supported by the Japan Society for The Promotion of Science (JSPS) Overseas Research
35 Fellowship and The Uehara Memorial Foundation research fellowship to ST; and the
36 Klingenstein Foundation, the Boettcher Foundation Webb-Waring biomedical research award
37 and NS084996 to ALP and the Neuroscience Training Grant (T32NS 099042 to JIG). Imaging
38 experiments were performed in the University of Colorado Anschutz Medical Campus Advance
39 Light Microscopy Core supported in part by Rocky Mountain Neurological Disorders Core Grant
40 Number P30NS048154 and by NIH/NCATS Colorado CTSI Grant Number UL1 TR001082.
41 Engineering support was provided by the Optogenetics and Neural Engineering Core at the
42 University of Colorado Anschutz Medical Campus, funded in part by the National Institute of
43 Neurological Disorders and Stroke of the National Institutes of Health under award number
44 P30NS048154.

JNeurosci Accepted Manuscript

45 **Abstract**

46 Cerebellar granule cells (GrCs) constitute over half of all neurons in the vertebrate brain and are
47 proposed to decorrelate convergent mossy fiber inputs in service of learning. Interneurons
48 within the granule cell layer, Golgi cells (GoCs), are the primary inhibitors of this vast
49 population and therefore play a major role in influencing the computations performed within
50 the layer. Despite this central function for GoCs, few studies have directly examined how GoCs
51 integrate inputs from specific afferents which vary in density to regulate GrC population
52 activity. We used a variety of methods in mice of either sex to study feedforward inhibition
53 recruited by identified MFs, focusing on features that would influence integration by GrCs.
54 Comprehensive 3D reconstruction and quantification of GoC axonal boutons revealed tightly
55 clustered boutons that focus feedforward inhibition in the neighborhood of GoC somata. Acute
56 whole cell patch clamp recordings from GrCs in brain slices showed that despite high GoC
57 bouton density, fast phasic inhibition was very sparse relative to slow spillover mediated
58 inhibition. Dynamic clamp simulating inhibition combined with optogenetic mossy fiber
59 activation at moderate rates supported a predominant role of slow spillover mediated inhibition
60 in reducing GrC activity. Whole cell recordings from GoCs revealed a role for the density of
61 active MFs in preferentially driving them. Thus, our data provide empirical conformation of
62 predicted rules by which MFs activate GoCs to regulate GrC activity levels.

63

64 **Significance Statement**

65 A unifying framework in neural circuit analysis is identifying circuit motifs that subserve
66 common computations. Widefield inhibitory interneurons globally inhibit neighbors and have
67 been studied extensively in the insect olfactory system and proposed to serve pattern separation
68 functions. Cerebellar Golgi cells (GoCs), a type of mammalian widefield inhibitory interneuron
69 observed in the granule cell layer, are well suited to perform normalization or pattern separation
70 functions but the relationship between spatial characteristics of input patterns to GoC mediated
71 inhibition has received limited attention. This study provides unprecedented quantitative
72 structural details of GoCs and identifies a role for population input activity levels in recruiting
73 inhibition using in vitro electrophysiology and optogenetics.

74

75 **Introduction**

JNeurosci Accepted Manuscript

76 A fundamental function of the cerebellar granule cell (GrC) is to decorrelate information
77 conveyed via convergent multimodal mossy fibers (MFs), increasing utility for learned
78 associations (Marr, 1969; Albus, 1971; Billings et al., 2014; Cayco-Gajic et al., 2017). Recent
79 work has demonstrated that GrCs receive and respond to MFs conveying diverse information
80 (Huang et al., 2013; Ishikawa et al., 2015) but little attention has been paid to the potential role
81 of multimodal integration by Golgi cells (GoCs). GoCs are in a key position to regulate
82 expansion recoding by GrCs since feedforward inhibition sets spiking threshold and thereby the
83 number of different afferents required to drive GrC firing (Marr, 1969; D'Angelo et al., 2013).
84 Indeed, theory suggests that feedforward inhibition via GoCs performs a thresholding-like
85 function, clamping the number of active GrCs at a relatively fixed level by engaging GoCs in a
86 scaled manner with increasing activity from MFs (Marr, 1969; Medina et al., 2000).
87
88 GoC inhibition of GrCs has been studied extensively in slices and is characteristically diverse.
89 Fast phasic IPSCs, a pronounced slow spillover-mediated component, and 'tonic'
90 $GABA_A$-receptor mediated currents are all forms of inhibition mediated by GoCs (for review,
91 see Farrant and Nusser, 2005; Nieus et al 2014; D'Angelo and De Zeeuw, 2009; Crowley et al.,
92 2009). The spill-over and tonic inhibitory tone within the layer would seemingly provide an
93 ideal mechanism for widely inhibiting the vast number of GrCs without necessarily forming
94 direct contact with each cell. Furthermore, relating GoC recruitment to the density of active
95 MFs is critical for testing the hypothesis of dynamic thresholding in service of pattern
96 separation.
97
98 Another challenge for GoCs is inhibiting the vast number of GrCs to regulate activity within the
99 granule cell layer. GoC axons are famously dense, but details of spatial ramification patterns
100 that define the likelihood of local GrCs sharing inhibition remain undefined. Indeed, the
101 problem of quantitatively addressing the distribution of inhibition from a single Golgi cell was
102 described by Ramon y Cajal: "When one of these axons appears completely impregnated in a
103 Golgi preparation, it is almost impossible to follow its complete arborization…. It is only in the
104 incomplete impregnations of adult animals … that one can study the course and divisions of the
105 axon. Ramon y Cajal 1890a" (Palay and Chan-Palay, 1974). To our knowledge, this observation
106 remains relevant in contemporary literature where all GoC reconstructions have been

JNeurosci Accepted Manuscript

107 incomplete (Simpson et al., 2005; Barmack and Yakhnitsa, 2008; Kanichay and Silver, 2008;
108 Vervaeke et al., 2010; Vervaeke et al., 2012; Szoboszlay et al., 2016; Valera et al., 2016).
109
110 To address these questions, we used a variety of methods to resolve GoC connectivity rules and
111 the capacity of specific afferents to produce fast phasic and slow spill-over mediated inhibition.
112 We performed comprehensive single cell, high-resolution reconstruction of GoCs with
113 quantitative morphological analysis to estimate glomerular innervation by GoCs. Optogenetic
114 activation of specific MF afferents from the pontine or cerebellar nuclei, which differ
115 systematically in their density, were used with electrophysiological recordings of GoCs from
116 slices to test the prediction that the density of afferent activity engages graded inhibition to
117 regulate GrC threshold.
118
119 **Materials and Methods**
120 ***Animals***
121 All procedures followed the National Institutes of Health Guidelines and were approved by the
122 Institutional Animal Care and Use Committee and Institutional Biosafety Committee at the
123 University of Colorado Anschutz Medical Campus. Animals were housed in an environmentally
124 controlled room, kept on a 12 h light/dark cycle and had *ad libitum* access to food and water.
125 Adult mice (2-5 months old) of either sex were used in all experiments; sex was not monitored
126 for experimental groupings. Genotypes used were C57BL/6 (Charles River Laboratories),
127 Neurotensin receptor1-Cre (Ntsr1-Cre; Mutant Mouse Regional Resource Center, STOCK Tg
128 (Ntsr1-cre) GN220Gsat/Mmucd) and GlyT2-eGFP (Salk Institute; Zwilhofer et al., 2005;
129 Tg(Slc6a5-EGFP)13Uze). All transgenic animals were bred on a C57BL/6 background and
130 maintained as heterozygotes. Ntsr1-Cre animals were genotyped for Cre, and GlyT2-eGFP
131 animals were genotyped for eGFP (Transnetyx).
132
133 ***Virus Injections***
134 For surgical procedures, at least one month old mice were anesthetized with i.p. injections of
135 ketamine hydrochloride (100 mg/kg) and xylazine (10 mg/kg) cocktail. Mice were placed in a
136 stereotaxic apparatus and bupivicaine (6 mg/kg) was injected along incision line. Craniotomies
137 were made above the cerebellar cortex (from lambda: -1.9 mm, 1.1 mm lateral, 1.2 mm ventral),

JNeurosci Accepted Manuscript

138 interposed nuclei (IN) (from lambda: -1.9 mm, 1.1 mm lateral, 2.4 mm ventral) and pontine
139 nuclei (from bregma: -3.7 mm, 0.5 mm lateral, 5.5 mm ventral). Pressure injections of virus
140 were administrated using a pulled glass pipette (7-9 µm tip diameter). Mice were allowed to
141 survive for more than 6 weeks before experiments, which we found in pilot experiments
142 optimized expression of reporter proteins in MF terminals.
143
144 ***Viruses***
145 AAV8-hSyn1-mCherry-Cre (titer: 10^2, UNC) and AAV2-CAG-FLEX-eGFP (titer: 10^{12}, Penn)
146 were coinjected to cerebellar cortex to sparsely label neurons for morphological analysis of
147 Golgi cells. AAV2-hSyn1-hChR2(H134R)-mCherry-WPRE (University of North Carolina
148 Vector Core) were injected to wildtype mouse IN and pontine nuclei to induce ChR2 expression
149 for electrophysiological recordings. AAV2- EF1a-DIO-hChR2(H134R)-mCherry-WPRE-pA
150 was injected into the IN of Ntsr1-Cre mice for a subset of nucleocortical MF studies (University
151 of North Carolina Vector Core).
152
153 ***Electrophysiology***
154 *Slice preparation*
155 At least 6 weeks after virus injection, mice were deeply anesthetized with isoflurane before
156 transcardial perfusion and slicing in warm (37-40 °C), oxygenated (95% O_2-5% CO_2) Tyrode's
157 solution containing (in mM): 123.75 NaCl, 3.5 KCl, 26 $NaHCO_3$, 1.25 NaH_2PO_4, 1.5 $CaCl_2$, 1
158 $MgCl_2$ and 10 glucose (Person and Raman, 2011; Ankri et al., 2014). Dissected cerebellum was
159 sliced at 300 µm in the coronal plane for Golgi cell recordings and either parasagittal or coronal
160 planes for granule cell recordings on a Leica VT1000S Vibratome. Slices were transferred to an
161 oxygenated Tyrode's solution (37°C) and incubated for 30-60 min.
162
163 *In vitro recordings*
164 One hour after slicing for granule cell recordings and immediately after slicing for Golgi cell
165 recordings (Hull and Regehr, 2012), tissue was transferred to the recording chamber.
166 Oxygenated Tyrode's solution (30 °C) was perfused over the slice at 3 ml/min and visualized
167 with Zeiss AxioExaminer equipped with xenon lamp LAMBDA DG-4 (Sutter Instrument) for
168 optogenetic stimulation through the objective. MFs were stimulated optogenetically with 2 ms

JNeurosci Accepted Manuscript

169 light pulses with a measured power of 18.5 mW at 473 nm (0.96-3.77 mW/mm^2 depending
170 diameter of the light cone at the preparation). Pulled glass patch electrodes (Golgi cell: 2-3.5
171 MΩ, Granule cell: 4 – 6 MΩ; Sutter Instruments, P-97) were filled with K-gluconate-based
172 internal solution containing the following (in mM): 120 K-gluconate, 2 Na-gluconate, 6 NaCl, 2
173 $MgCl_2$, 1 EGTA, 4 Mg-ATP, 0.3 Tris-GTP, 14 Tris-creatine phosphate, 10 HEPES, and adjusted
174 for pH (7.3) with KOH and osmolarity (290 mOsm) with sucrose. For all Golgi cell recordings
175 and a subset of granule cell recordings, biocytin (0.3%; Tocris Bioscience) was added to the
176 internal solution. Whole-cell recordings were made in current-clamp and voltage-clamp mode,
177 low-pass filtered at 6-10 kHz, amplified with a MultiClamp 700C, partially compensated for
178 series resistance, digitized at 10-50 kHz with a Digidata 1550 and monitored with pClamp
179 acquisition software (Molecular Devices). Blockade of neurotransmitter receptors was achieved
180 with bath application of 10 µM RS-CPP (Tocris Bioscience) to block NMDARs, and 10 µM
181 SR95531 (Tocris Bioscience) to block $GABA_A$Rs. Data were analyzed with custom routines
182 and with the Neuromatic package (ThinkRandom) in IGOR Pro (Wavemetrics; RRID:
183 SCR_000325). We targeted recordings to locations of ChR2 expression in mossy fibers,
184 particularly Crus 1, 2, Lobule Simplex, and Lobule 4/5.
185
186 *Dynamic clamp*
187 Dynamic clamp experiments were performed using a custom built microcontroller-based
188 dynamic clamp system with 10 µs input-output latency (Desai et al., 2017; dynamicclamp.com).
189 We modified the layout, customized resistors, and made a custom 3D printed enclosure, and
190 calibrated the system with details provided as an open resource from the Optogenetics and
191 Neural Engineering Core at the University of Colorado Anschutz Medical Campus with
192 modifications publically available. Simulated current timing was triggered by TTL via a
193 Master-8 Pulse Stimulator (A.M.P.I).We simulated both mossy fiber EPSCs and GoC mediated
194 IPSCs, with parameters calculated from our GrCs recording data set using optogenetic
195 stimulation of mossy fibers as well as previous reports (Rossi and Hamann, 1998). Dynamic
196 clamp IPSGs mimicked $GABA_A$ receptor- mediated conductances with a reversal potential of
197 -70 mV and a linear ohmic current-voltage relation, with kinetics following a single exponential
198 rise and decay model as follows: Fast phasic IPSGs had a 2.15 ms rise time, 2.29 ms τ_{decay}, and
199 a peak conductance of 0.3 nS (small) or 1.2-1.5 nS (large). Slow phasic IPSGs had a 30.2 ms

JNeurosci Accepted Manuscript

200 rise time, 630 ms τ_{decay}, and peak conductances of 0.032 or 0.32 nS. These reflected
201 observations made in a subset of recordings in which trains of mossy fiber stimuli were made
202 while recording IPSCs in GrCs (Fig. 5). Both depressing and non-depressing synapses were
203 mimicked. Depressing synapses reflected previous reports from in vivo recordings, where
204 IPSGs rapidly depressed to approximately 50% after the first IPSG in a burst (Duguid et al.,
205 2015). Dynamic clamp mimicking mossy fiber-like EPSGs were delivered at 100 Hz and
206 depressed to a steady state of 50% across trains (Saviane and Silver, 2006). Each EPSG
207 followed an excitatory synaptic model with peak conductance of 1.5 nS, 0.4 ms rise time and
208 decay time of 1.3 ms and had a net reversal potential of 0 mV, reflecting dual AMPA and
209 NMDA receptor mediated conductances as described previously (Walcott et al., 2011).
210
211 ***Tissue preparation for light microscopy***
212 Mice were overdosed with an intraperitoneal injection of a sodium pentobarbital solution, Fatal
213 Plus (Vortech Pharmaceuticals), and perfused transcardially with 0.9% saline followed by 4%
214 paraformaldehyde. Brains were removed and postfixed for at least 24 hrs then cryoprotected in
215 30% sucrose. Tissue was sliced in 40 µm serial coronal sections using a freezing microtome and
216 stored in 0.1 M PB.
217
218 For post hoc morphological analyses following slice electrophysiology, tissue was transferred to
219 warm 4% paraformaldehyde and postfixed for less than 3 hrs then placed in 30% sucrose.
220 Tissue was rinsed in 0.1M PB for 30 min then treated in 0.3% Triton X-100 in 0.1M PB for 2
221 hrs followed by three washes in PB (10 min each). To visualize biocytin, tissue was incubated
222 with streptavidin conjugated to AlexaFluor 647 or 555 (Life Technologies) diluted 1:100 in 0.1
223 M PB overnight at 4 °C followed by three washes in PB (20 min each).
224
225 ***Imaging***
226 Confocal images were obtained using Zeiss LSM 780. To reconstruct all processes and/or map
227 all axonal boutons of GoCs, sequential images were taken with diffraction limited resolution
228 achieved via 63x oil objective with NA1.4. (Plan-Apochrom 63x/1.4 oil DIC M27 objective by
229 Ar-Iron laser; 0.39 µm z step). This achieved a computed x,y resolution of 175 nm for the 488
230 nm signal and 200 nm for 561 nm signal, based on the relationship $Res_{(x,y)} = \lambda/2NA_{Obj}$. For MF

JNeurosci Accepted Manuscript

231 density analysis images of filled cells were collected and density analyzed within 53,615±5,180
232 μm^2 of the GoC soma. Images examining MF proximity to GoCs were visualized in Zen
233 software using transparent rendering mode. High resolution imaging for GlyT2-GFP boutons
234 was performed with a Nikon A1r-HD confocal with a Plan Apo 60x oil objective, NA 1.4.
235 Deconvolution was performed in NIS-Elements C imaging software.
236
237 ***Morphological analysis***
238 GoC reconstructions were performed using Neurolucida 360 software (MBF Bioscience; RRID:
239 SCR_001775). Reconstructed GoCs were located in vermal lobule 4/5. Processes were traced in
240 user-guided mode. Fine grained reconstructions captured axonal and dendritic swellings by
241 adjusting points along processes to match thickness. Because individual GoCs spanned multiple
242 sections, each section was individually reconstructed, then each reconstructed section was
243 stacked using morphological landmarks visible across sections, such as the Purkinje cell layer.
244 To define the relative extent of basal axons and dendrites, we traced these processes with
245 attention to process thickness and contours. Axons were characterized by their smaller diameter
246 (~0.2 µm) and were studded with boutons (~3 µm diameter). For all analyses of reconstructed
247 GoC morphological features, we used Neurolucida Explorer. To define the GCL volume
248 occupied by the cell, we computed the convex hull volume which calculates the volume of a
249 convex polygon connecting the tips of the distal processes. To map boutons, we used
250 Neurolucida 360 and placed markers on each bouton by with 0.39 µm z resolution. All images
251 were aligned and coordinates of boutons were exported and processed in Matlab (RRID:
252 SCR_001622). Nearest Boutons: All distance analyses used Euclidean distance. Nearest bouton
253 color maps were constructed as 3D-scatter plots in Matlab. Bouton distance probabilities were
254 computed in 0.2 µm bins and normalized by the total number of boutons. Comparisons of
255 bouton density between single Golgi cells and global GlyT2-GFP label was calculated by first
256 computing the local density of boutons for single GoCs, defined as the number of boutons
257 within a 25 µm radius sphere of each bouton. The density of GlyT2 boutons was determined by
258 mapping boutons in 6 GlyT2-GFP GCL samples and dividing the total bouton count by the
259 volume of the image. Density measurements were then compared between single GoCs and the
260 GlyT2-GFP+ population by computing the ratio of bouton densities in a single GoC and mean
261 GlyT2-GFP bouton density. The ratio was used to estimate the fraction of bouton density

JNeurosci Accepted Manuscript

262 accounted for by a single GoC. We display the distribution of density ratios in a histogram
263 normalized by the total number of boutons with a bin size of 0.05.
264

265 ***Experimental design and Statistical analysis***

266 Paired and unpaired t-tests were performed using RStudio (version 1.0.136; RStudio). Linear
267 regression analysis was performed using GraphPad Prism 7.04 and Matlab (GraphPad software;
268 RRID:SCR_002798). Statistical tests are specified in the text. Electrophysiological and
269 morphological analyses are described above.
270

271 **Results**

272 ***Spatial distribution of Golgi cell processes***

273 Rules of integration in GrCs will depend critically on the structure of feedforward inhibition
274 within the granule cell layer (GCL). Previous studies have proposed contradictory integrative
275 models. Influential older work proposed that GoC axons tile the GCL in a non-overlapping
276 manner such that GrCs are innervated by a single GoC (Eccles et al., 1967), yet physiological
277 measurements estimated convergence of multiple GoCs onto GrCs but the existence of slow
278 spillover current makes convergence estimates challenging (Rossi and Hamann, 1998). Several
279 morphological features of GoCs, including axonal volume and bouton density, are each
280 essential to infer the inhibitory convergence in the GCL. Therefore, we set out to define the
281 density of GoC basal axons to test these assumptions and inform inhibitory connectivity rules in
282 the GCL. We performed comprehensive basal arbor reconstruction to quantify GoC
283 morphological characteristics that contribute to spatial distribution of feedforward inhibition in
284 the GCL. To do so, we used a sparse viral labeling technique which restricted the number of
285 fluorescent GoCs in cerebellar cortex. A combination of low titer Cre recombinase-expressing
286 virus (AAV8-hSyn1-mCherry-Cre; titer: 10^2) and high titer Cre-dependent reporter virus
287 (AAV2-CAG-FLEX-eGFP; titer: 10^{12}) were injected into cerebellar cortex which resulted in
288 very sparse labeling of individual GoCs (Fig. 1A).

289 In keeping with previous reports, sparse GoC label revealed extensive basal axons, which were
290 characterized by their small diameter (~0.2 µm) (Palay and Chan-Palay, 1976; Holtzman et al.,
291 2006; Barmack and Yakhnitsa, 2008; Hull and Regehr, 2012; Vervaeke et al., 2012; Ankri et al.,

JNeurosci Accepted Manuscript

292 2015; Valera et al., 2016). An example GoC is shown in Fig. 1B. This GoC extended processes
293 ~200 µm mediolaterally, ~330 µm dorsoventrally, and ~180 µm rostrocaudally, occupying a
294 convex hull volume – or the volume of space occupied by the boundaries of the axonal field, as
295 if a sheet were draped around it -- of approximately 5.7×10^6 µm^3 and overall axonal length of
296 26.7 mm (Neurolucida; see Methods). Therefore, this GoC basal axon encompasses a volume
297 that contains approximately 15,000 GrCs and 580 MF rosettes (MFRs) based on estimates of
298 GrC and MFR densities (Palkovits et al., 1971). GoC basal dendrites were distinguishable from
299 axons by their larger diameter (0.3 – 3.2 µm) and smooth surface devoid of boutons as previous
300 described (Palay and Chan-Palay, 1974; Hull and Regehr, 2012; Vervaeke et al., 2012; Ankri et
301 al., 2015; Rudolph et al., 2015; Szoboszlay et al., 2016). Dendrites comingled with axons but
302 were considerably shorter (Fig. 1C, right), with a length totaling 1.4 mm (Fig. 1D) and
303 encompassing a computed volume of 0.41×10^6 µm^3 (Fig. 1 E; convex hull volume;
304 Neurolucida, see Methods). Because the total axon processes was ~20 times longer than basal
305 dendrites, GoC mediated inhibition is predicted to be distributed more widely than the afferent
306 input in the GCL, as has been previously noted (D'Angelo et al., 2013).

307 The highly restricted cell labeling *in vivo* also permitted novel quantification of GoC bouton
308 density and numbers. Axons possessed distinct bouton swellings (~3 µm diameter). We
309 comprehensively mapped boutons of four complete GoCs located in vermal lobule 4/5 and
310 quantified bouton density of an additional partially reconstructed GoC (Fig. 1F), which was
311 included in a subset of analyses. Axons of individual GoCs were studded with a total of
312 6,000-7,500 boutons (5.9×10^3 - 7.46×10^3), for an average single GoC bouton density of
313 4.34×10^5 boutons/mm^3 (n = 4 from four mice). We calculated the nearest bouton by Euclidean
314 distance, which revealed that a majority (74 – 93%) were within 4 µm of another bouton from
315 the same cell (Fig. 2A-C; median nearest bouton, 2.18-3.39 µm; n = 27,402 boutons from 4
316 cells). The distance from each bouton to its nearest within-cell neighbor remained fairly
317 constant across the axonal arbor (Fig 2C), illustrated in the color map of nearest neighbors. We
318 quantified this observation with linear regressions relating the nearest bouton distance to its
319 position relative to the soma on a per-cell basis (Ranges across cells: R^2=0.0005-0.2, all $p<0.01$,
320 F=3.25-54, DF=1893-7811, n=5). Although the nearest boutons remained fairly constant across
321 the axonal arbor, visual inspection of the bouton maps suggested clustering toward the soma.

JNeurosci Accepted Manuscript

322 We therefore analyzed the number of neighbors within 10 μm of each bouton. This analysis
323 revealed highly structured clustering, where a majority of boutons close to soma had more than
324 20 close neighbors from the same cell. This clustering dropped as a function of distance from
325 the soma (Fig. 2D, E; R^2=0.05-0.35, all $p<0.01$, F=213-3,100, DF=1893-7811, n=5).

326 These comprehensive bouton maps allowed us to estimate GoC overlap at the glomerulus. To
327 do so, we first compared bouton distributions from single cell reconstructions with those
328 observed in GlyT2-eGFP mice, which label approximately 85% of GoCs (Fig. 3A) (Simat et al.,
329 2007). Mapping boutons in these preparations revealed an overall bouton density of $6.54x10^6$
330 boutons/mm^3. Distributions of nearest boutons differed slightly between single cell
331 reconstructions and GlyT2-eGFP label (Fig. 3B). Not surprisingly, GlyT2-eGFP labeled
332 boutons were more closely spaced, with a prominent peak at ~ 1.5 μm compared to the peak at
333 3 μm for the single neurons. Differences between single cells and the population were more
334 pronounced when looking at local clustering, seen by measuring the distances to the closest 10
335 neighbors (Fig. 3C). GlyT2-eGFP labeled boutons were denser, with the closest 10 boutons
336 appearing on average ~4 μm away from every other bouton from the same cell. By contrast, the
337 nearest 10 boutons to each bouton on axons from individual neurons averaged ~7 μm. These
338 analyses allowed us to estimate how many GoC axonal arbors overlap locally. To estimate GoC
339 axonal overlap, we examined the proportion of GlyT2-GFP positive bouton density accounted
340 for by a single GoC. In areas within 50 μm of a GoC soma, single GoC axons tended to account
341 for 40-85% of bouton density, suggesting that glomeruli here are likely dominated by a single
342 GoC (Fig. 3D). Nevertheless, the proportion of population bouton density accounted for by a
343 single GoC falls off with distance from the GoC soma, as indicated with significant negative
344 slopes of regressions (Fig. 3D; R^2 = 0.29-0.66; $p<0.0001$; F= 768-11600; df, 1895-7811, n=5).

345 The distribution of single GoC: GlyT2 bouton density (Fig. 3E) can be viewed as an estimate of
346 the distribution of the number of overlapping GoCs. The peak in the distributions near 0.2
347 (mean 0.22 ± 0.05 for complete reconstructions), indicating that a typical degree of overlap
348 between GoCs is around 5. Assuming that 15% of GoC boutons remain unlabeled in
349 GlyT2-GFP mice, shifts the distribution slightly, to peak around 0.18, suggesting between 5 and
350 6 overlapping GoCs is common. Notably, the broad distribution around the peaks indicates a

JNeurosci Accepted Manuscript

351 large variance in the number of overlapping GoCs at any position, ranging from 2-20 as
352 extremes.

353 ***Low probability fast phasic feedforward inhibition in the GCL***

354 The spatial extent of GoC processes position them as sites of MF convergence and inhibitory
355 divergence, motivating experiments examining how feedforward inhibition is recruited by
356 identified cerebellar inputs. To begin to test how diverse MF afferents interact in the GCL, we
357 first scaled down the question to address how identified sources of information recruit GrCs and
358 feedforward inhibition via GoCs. We examined uni-modal information processing of GrCs by
359 recording postsynaptic currents evoked by optogenetic stimulation of a subset of MFs
360 originating from neurons in the cerebellar nuclei, known as the nucleocortical (NC) MFs or
361 those originating in the pontine nuclei. AAV2-hSyn1-hChR2-mCherry-WPRE-PA (See
362 Methods) was injected into either the interposed nucleus (IN) or pontine nuclei to express ChR2
363 in MFs. In a small subset of experiments, AAV2- EF1a-DIO-hChR2(H134R)-mCherry was
364 injected into the IN of Ntsr1-Cre mice, to manipulate the nucleocortical pathway. MF density
365 averaged 3673 ± 1911 rosettes/mm^3 (n = 7 from 5 mice), thus NC pathway inputs were sparsely
366 spaced, as described previously (Gilmer and Person, 2017). We examined the GrC responses to
367 MF optogenetic stimulation in an acute brain slice preparation from adult mice. We isolated
368 EPSCs and IPSCs by holding GrCs at -70 mV or 0 mV respectively and stimulated ChR2
369 expressing MFs at between 20 - 60 Hz with blue light pulses delivered through the objective
370 (Fig. 4A; 2 ms pulses; 0.96-3.77 mW/mm^2).

371 EPSCs evoked from optogenetic excitation of the NC had an average amplitude of 80.6 ± 9.3
372 pA (Fig. 4B, F; sem; n = 7) and 10-90% rise and 37% decay times typical of AMPA type
373 glutamate receptor-mediated currents in granule cells, averaging 0.25 ± 0.04 ms and 1.0 ± 0.2
374 ms respectively, similar to group 2 excitatory inputs previously described (Chabrol et al., 2015).
375 Surprisingly, however, given the large spatial convergence of MFs and subsequent divergence
376 of inhibition within the GCL fast phasic IPSCs recorded at 0-3 mV holding potentials were
377 uncommon, observed in just 5/12 responsive GrCs and 5/96 total GrCs (Fig. 4C, G from N=11
378 and 18 mice respectively). Fast phasic IPSCs were distinct from EPSCs, with smaller
379 amplitudes and slower kinetics, averaging 40.3 ± 5.5 pA, with 0.9 ± 0.1 ms 10-90% rise times

JNeurosci Accepted Manuscript

380 and 2.7 ± 0.4 ms 37% decay times (Fig. 4I; n = 5; EPSC vs IPSC amplitude, p=0.007; rise time,
381 p < 0.001; decay time, p = 0.001; unpaired t-tests). These measurements were statistically
382 indistinguishable from spontaneous fast phasic inhibitory currents (amplitude, p = 0.1; rise time,
383 p = 0.3; decay time, p = 0.2; unpaired t-tests), suggesting they originate from single GoCs
384 rather than recruitment of multiple convergent GoCs. Moreover, as expected for feedforward
385 inhibition, IPSC latencies and temporal variability were distinct from those of EPSCs (Fig. 4D),
386 averaging 13.5 ± 0.9 ms vs 4.2 ± 0.3 ms for EPSCs, with latency jitter (SD of latency)
387 averaging 3.6 ± 0.7 ms versus 0.29 ± 0.2 ms for EPSCs (Fig. 4E; p < 0.001; unpaired t-test).
388 Thus, fast phasic inhibition observed in GrCs following NC optogenetic stimulation had the
389 hallmark of feedforward inhibition mediated through GoC recruitment but was nevertheless
390 uncommon.

391 Given the shared sparseness of direct excitatory and disynaptic phasic inhibitory inputs to GrCs
392 following NC stimulation, we next examined the overlap of these inputs onto single GrCs. As
393 expected for sparse synaptic contacts, GrCs with phasic responses to NC pathway stimulation
394 showed either EPSCs (58.3%) or fast phasic IPSCs (41.6%) but not both in our recording set
395 (Fig. 4I). When NC EPSCs were elicited at -70 mV, no fast phasic IPSC was detectable holding
396 the cell at 0 mV; conversely, when IPSCs were evident at 0 mV, no EPSC was detectable at -70
397 mV.

398 Slow spillover-mediated inhibition has been proposed as the primary form of inhibition within
399 the GCL, so we next examined GrCs for slow inhibitory currents. Slow inhibitory currents were
400 observed in all GrCs with phasic excitatory or inhibitory responses, with an average charge
401 transfer of 124.5 ± 21 (pA·ms; IPSC area) (Fig. 4H, J). Thus, slow phasic inhibition dominates
402 feedforward inhibitory processing from identified MF pathways, consistent with observations
403 from electrical stimulation.

404 To contrast experiments studying low density of MFs from the NC pathway, we next examined
405 GrC responses to a dense MF population originating in the pontine nuclei with optogenetics
406 (Huang et al., 2013; Gilmer and Person, 2017). Labeled pontine MFs were dense, averaging
407 107,749 ± 27,965/ mm^3 (sd) n = 10 in 5 mice. We made whole cell patch clamp recordings of
408 GrCs in the vicinity of labeled MFs. Light stimulation evoked excitatory or fast phasic

JNeurosci Accepted Manuscript

409 inhibitory currents in 21 GrCs in 8 mice (Fig. 4K, L, M; EPSCs, 55.6 ± 7.6 pA, with 0.4 ± 0.03
410 ms 10-90% rise times and 1.3 ± 0.11 ms 37% decay times, 2.8 ± 0.2 ms latency (n=18); IPSCs;
411 22.2 ± 1.2 pA, with 2.2 ± 0.4 ms 10-90% rise times and 2.3 ± 0.5 ms 37% decay times; 12.8 ±
412 2.1 ms latency (n=8)). The fraction of overlap of phasic EPSCs and fast phasic IPSCs was
413 higher with pontine stimulation, as expected of a denser input: EPSCs without phasic IPSCs
414 were evoked in 62% of GrCs and exclusively phasic IPSCs were evoked in 14% of recorded
415 GrCs, constituting 76% of responsive cells. In the remaining 24% of responsive neurons,
416 pontine MF stimulation evoked both EPSCs and fast phasic IPSCs (5/21) (Fig. 4O). Thus,
417 density of MF afferents influences the overlap between phasic excitation and inhibition. As was
418 observed for NC fibers, however, slow inhibitory currents dominated fast phasic inhibition, and
419 were seen in all cells with phasic currents following pontine MF activation, with an average
420 charge transfer of 88 ± 8.0 (pA·ms) (Fig. 4N, P).

421 To summarize, fast phasic inhibition was probabilistically recruited onto GrCs depending on the
422 approximate density of MF terminals but slow inhibitory currents were much more widespread,
423 even when evoked by a sparse MF input.

424 ***Predominant role of slow spillover inhibition in regulating GrC excitability***
425 GoC-mediated feedforward inhibition has been proposed to regulate the number of mossy fibers
426 necessary to recruit GrCs. We tested the efficacy of physiological levels of feedforward
427 inhibition regulating GrC excitability, combining optogenetic stimulation of pontine MFs and
428 dynamic clamp, mimicking physiologically realistic feedforward fast and slow phasic inhibitory
429 conductances (N = 12 mice). We recorded from GrCs in the presence of SR95531 (10 μM) to
430 block endogenous $GABA_A$ receptors. In whole cell current clamp mode, we measured GrC
431 firing in response to 20 Hz optogenetic stimulation of pontine MFs, followed by delayed fast
432 phasic IPSGs or slow phasic IPSGs produced via the dynamic clamp, mimicking GoC-mediated
433 feedforward inhibition. GrCs were held at -60 to -75 mV by current injection to promote
434 MF-driven firing. We used two conductances for both fast and slow phasic currents, with the
435 lower of the two matching physiologically measured values but the higher providing insight
436 into the upper bound of physiological levels of inhibition.
437
438 Low conductance fast phasic IPSGs (0.3 nS; rise time 2.15 ms, decay tau 2.29 ms),

JNeurosci Accepted Manuscript

439 approximating a single fast phasic GoC input, were delayed by 12.8 ms relative to light in a 20
440 Hz light pulse 500 ms train to approximate feedforward inhibition. Across the population, this
441 manipulation did not significantly change optogenetically driven firing compared to optogenetic
442 stimulation alone (Fig. 5A, B; -3.9 ± 2.3 Hz from baseline, $p > 0.1$, paired t-test; n=8), although
443 in one cell fast phasic IPSGs significantly reduced MF-driven firing responses (1/8 cell; -10.8
444 Hz from baseline, pontine 81.8 ± 2.0 sp/s, pontine + IPSG 71.0 ± 1.8 sp/s, unpaired t-test, n=10
445 pontine; n=5 pontine + IPSG trials; p=0.002). As a positive control, we next tested whether
446 stronger phasic inhibition influenced firing rate. We increased the magnitude of the phasic
447 stimulation to 1.2 nS, which is physiologically unlikely, since fast phasic contacts are rare and
448 this assumes 4 onto a single cell, when only 60% of GrC dendrites receive direct contacts
449 (Jakab and Hamori, 1988; Rossi and Hamann, 1998). As expected, this manipulation reduced
450 response frequency (Fig. 5C, D; -11.9 ± 3.4 Hz from baseline, $p < 0.05$, paired t-test, n=8), with
451 significant effects seen in 4/8 cells ($p < 0.05$, unpaired t-test, n=10 pontine; n=5 pontine + IPSG
452 trials in each cells).
453
454 Because mossy fibers are known to burst at much higher rates, over 100 Hz, we also examined
455 the role of phasic inhibitory currents to reduce excitability to higher frequency stimuli.
456 Optogenetic probes are not well suited to follow such high rates, so we used a dynamic-clamp
457 only approach to mimic both excitation and inhibition. At high rates, GoC inhibitory currents
458 also depress, so we combined high frequency (100 Hz; 1.5 nS peak conductance) EPSGs, which
459 depressed to approximately 50% of their max amplitude after three stimuli, (Saviane and Silver,
460 2006), and high frequency IPSGs (60 Hz); which depressed to 50% after one stimulus (Duguid
461 et al., 2015). Both physiological and large fast phasic inhibitory currents also significantly
462 reduced response rates in some neurons (Fig. 5B, D; $p < 0.05$ for 4/11 neurons, mean rate
463 change -0.9 ± 1.5 spikes/s 0.3 nS peak; $p < 0.05$ 8/9 cells, mean rate change -19.6 ± 4.6 spikes/s,
464 1.5 nS peak).
465
466 In previous dynamic clamp studies, slow spillover-like inhibitory currents attenuated GrC firing
467 more effectively than fast phasic IPSCs (Crowley et al., 2009). We extended these experiments
468 to explicitly test a role for feedforward inhibition, such that the slow current was delayed
469 relative to excitation and used conductances mimicking current from a single GoC or higher

JNeurosci Accepted Manuscript

470 conductances that reflect summated slow phasic inhibition. We first mimicked slow phasic
471 inhibition observed during 50 Hz light trains to stimulate mossy fibers (Fig. 5E, bottom trace),
472 injecting IPSGs (0.032 nS) following the first light stimulation, again delayed by 12.8 ms. This
473 experimental condition did not reduce MF driven firing rates (Fig. 5E -4.4 ± 2.2 Hz from
474 baseline, $p > 0.05$, paired t-test, n=8). Because multiple GoCs converge in a glomerulus we next
475 tested higher conductance IPSGs that reflect summated slow phasic inhibition. We therefore
476 increased conductance 10 fold capturing summation. As expected, larger slow phasic IPSGs
477 (0.32 nS) strongly attenuated rates in most GrCs (Fig. 5G, H, 7/8 cells, $p<0.05$, unpaired t-test,
478 n=10 pontine; n=5 pontine + IPSG trials in each cells).
479

480 ***GoC recruitment scales with MF input density***

481 The dynamic clamp experiments indicate that fast phasic feedforward inhibition from GoCs
482 regulates the threshold of GrCs (Brickley et al., 1996; Wall and Usowicz, 1997; Rossi and
483 Hamann, 1998; Hamann et al., 2002; Mitchell and Silver, 2003). Threshold regulation was a
484 major role for GoCs in theoretical studies proposing a role for pattern discrimination by GrCs,
485 and predict that GoC recruitment would scale with input density (Marr, 1969; Pellionisz and
486 Szentagothai, 1973; Mapelli et al., 2009; Honda and Ito, 2017). Therefore, identifying rules of
487 GoC recruitment is essential to differentiate between diverse models of GrC information
488 processing.
489

490 To better understand the rules of GoC recruitment by identified MF inputs, we next recorded
491 from GoCs directly, measuring evoked firing and synaptic currents following optogenetic
492 stimulation of MFs originating in the cerebellar or pontine nuclei (Fig. 6A). We used
493 GlyT2-eGFP mice to identify GoCs under fluorescence, noting that this excludes a small
494 subpopulation of GoCs from our dataset (Simat et al., 2007). We first tested the efficacy of
495 EPSPs from both NC and pontine sources to drive firing in GoCs in current clamp mode during
496 trains of stimuli delivered at rates between 20-60 Hz (Fig. 6C). GoCs were spontaneously active
497 during patching, with firing rates spanning 2.4 - 47.5 spikes/s. We performed linear regression
498 analysis on firing rate changes as a function of stimulation frequency. Consistent with previous
499 observations from electrical stimulation (Kanichay and Silver, 2008), MF stimulation rates
500 were poor predictors of firing rate changes across the population ($R^2 = 0.03$, p= 0.03, F= 4.6,

JNeurosci Accepted Manuscript

501 df= 176, n=178 from 36 cells pooled; N=23 mice).

502

503 This filtering property has been previously ascribed to a large afterhyperpolarization from
504 EPSP-driven spikes (Kanichay and Silver, 2008). Nevertheless, it raises the question of how
505 GrC population activity could remain constant if GoC recruitment is strongly filtered,
506 prompting us to look closer at the relationship between MF activity and GoCs. Indeed, when we
507 examined the relationship of firing rate with stimulation rate in individual neurons, we noted
508 that some were strongly correlated, with significant within-cell correlation (Fig. 6F; $p<0.04$,
509 n=7) while many cells were not (Fig. 6E; $p>0.05$, n=28). We next examined whether properties
510 of the EPSCs differed between these groups and found a strong bias toward stronger EPSCs
511 supporting linear input-output relations (Fig. 6G; 332.1 ± 41.5 pA, n=7). Weaker EPSCs, by
512 contrast, did not modulate GoC spike rates with increasing stimulus rates (Fig. 6G; 71.5 ± 8.1
513 pA, n=35).

514

515 These findings indicate that EPSC amplitude determines the input filtering properties of GoCs.
516 To identify factors that influence the amplitude of EPSCs onto GoCs, we took advantage of the
517 fact that optogenetic probes are coupled with a fluorophore, thus we could directly measure the
518 density of activated inputs. This allowed us test the prediction that MF convergence onto GoCs
519 from multiple inputs would summate to regulate EPSC amplitude in GoCs. Consistent with
520 high levels of convergence of MFs onto GoCs, there was a strong linear relationship between
521 MF density and EPSC amplitude, with higher density MFs eliciting larger EPSCs (Fig. 6H; $R^2=$
522 0.44, p=0.001, F=14.3, df=18, n=20). Despite the sparseness of NC MFs, which constitute just
523 1-10% of local MFs (Gilmer and Person, 2017), optogenetic activation of the pathway at 40 Hz
524 elicited EPSCs in 35% of GoCs recorded in the vicinity of labeled MFs (34/96). Denser MF
525 populations from the pontine nuclei elicited responses in 87% of nearby GoCs (14/16). Not
526 surprisingly, given the large difference in density between pontine and NC inputs pontine inputs
527 elicited significantly larger EPSCs ($p<0.001$, unpaired t-test, -259.5±26.8 pA, n=70 from 14
528 cells pooled, -40.7±3.1 pA, n=131 from 28 cells pooled, respectively). These observations
529 suggest that GoCs integrate many inputs from diverse sources and are responsive to the level of
530 input population activity as expected for active thresholding.

531

JNeurosci Accepted Manuscript

532 Having identified a relationship between MF input density and GoC EPSC amplitude and
533 linearity of firing responses, we next reasoned that GoC firing responses might be sensitive to
534 the overall level of MF activity levels, i.e. the density of active inputs. We tested this idea by
535 analyzing the density of MFs labeled within the vicinity of the recorded GoC, and relating
536 measurements to the magnitude of firing rate changes observed with 40 Hz stimulation. In
537 keeping with this reasoning, we found a positive significant correlation between active input
538 density and the magnitude of firing rate changes during stimulation (Fig. 6I; $R^2 = 0.23$; p=0.04;
539 F= 5.0; df= 16; n= 18).
540
541 As described in previous studies (Kanichay and Silver, 2008; Hull and Regehr, 2012; Cesana et
542 al., 2013; Gao et al., 2016), there was considerable diversity in GoC EPSC properties, which
543 differed by amplitude, latency and whether they were singular or included disynaptic feedback
544 via ascending and parallel fiber input from GrCs. In general, EPSCs fell into three broad classes,
545 which included (1) short latency; (2) mixed short- and long-latency producing multiple peaks
546 per stimulus; (3) and long-latency (Fig. 6D). Consistent with the view that these response
547 classes reflect mono and di-synpatic input, biocytin fills of recorded GoCs revealed ChR2-RFP
548 expressing MF inputs adjacent to somata and/or basal dendrites of short-latency responders,
549 defined as those with responses occurring within 3.6 ms. Nine of 11 short-latency responders
550 were histologically recovered. In the case of long-latency responders (those with responses >
551 3.8 ms), no MF inputs were identified adjacent to the somata or basal dendrites (Fig. 6B; n= 3
552 of 3 recovered GoCs with long latency responses). Furthermore, bath application of the NMDA
553 receptor antagonist CPP reduced the likelihood of multipeaked EPSC being elicited from 37.9 ±
554 14.0 % to 5.8 ± 1.0 % (n=3 cells; N = 3 mice), supporting the view that late synaptic responses
555 were the result of disynaptic recruitment of GrCs (Cesana et al., 2013).
556
557 Because GoC multipeaked EPSCs are a readout of GrC recruitment which is in turn regulated
558 by GoC inhibitory feedback (Cesana et al., 2013), we reasoned that we could use the
559 relationship between MF input strength and multipeaked EPSC probability to test whether
560 GoCs dynamically modulate MF-GrC gain as predicted in numerous models (Mitchell and
561 Silver, 2003). GoC EPSC multipeak probability was linearly correlated with the initial EPSC
562 amplitude (Fig. 6J; R^2=0.41, p<0.0001, F=27.9, DF=40, n=42), indicating that stronger input

JNeurosci Accepted Manuscript

563 recruited more GrCs. Interestingly, however, there was no detectable change in multipeak
564 probability or number of peaks over the course of moderate frequency (40 Hz) stimulus trains
565 ($p = 0.68$, $p = 0.65$, paired t-test of early vs late train multipeak probability or early vs late train
566 number of peaks per stimulus). This stability of multipeak probability was evident regardless of
567 whether multipeak probability was high or low at the beginning of the stimulus train. Coupled
568 with the observation that $GABA_A$ receptor blockade strongly enhances multipeak probability
569 (Cesana et al., 2013), these findings indicate that feedback inhibition within the layer stabilizes
570 GrC excitability for a given input excitation level.
571
572 **Discussion**
573 This study used a combination of quantitative morphometry, optogenetics and dynamic clamp
574 to test theoretical predictions about GoCs as global regulators of GrC excitability. Theory has
575 long posited a role for GoCs in regulating GrC population activity (Eccles et al., 1967; Marr,
576 1969), proposing that they respond dynamically to varying input levels to modulate all local
577 GrC thresholds, but data testing key assumptions of this view have been lacking. Here we
578 confirm theoretical predictions that GoC axons are ideally suited to globally inhibit neighboring
579 GrCs; that spillover-mediated feedforward inhibition alters GrC thresholds; and that convergent
580 afferents are essential to recruit GoC inhibition in a manner consistent with a global 'listening'
581 mechanism well suited for normalizing activity in the GCL. These data indicate that the large
582 multimodal integrative capacity of the GoC, combined with physiological integrative rules of
583 GrCs set up a MF activity level-detector to regulate inhibition levels within the GCL.
584
585 GrCs have been proposed to perform pattern separation by sparsening information conveyed by
586 MF inputs (Cayco-Gajic et al., 2017). Inhibition from widefield interneurons has been proposed
587 in both mammalian cerebellum and other systems to perform these computations (Pouille et al.,
588 2009). An underlying but untested assumption is that inhibitory interneurons contact all or
589 nearly all neurons in the field to effectively regulate population activity (Marr, 1969; Albus,
590 1971; Billings et al., 2014; Duguid et al., 2015; Cayco-Gajic et al., 2017). Similar roles have
591 been proposed for cerebellar GoCs. However, although their morphology has long been
592 appreciated as complex and suitable for widespread inhibition, quantitative analysis of axonal
593 bouton density has not been performed, leading to conflicting speculation about whether

JNeurosci Accepted Manuscript

594 inhibition they produce is spatially structured. Our morphometry shows that GoCs are suited to
595 contact every nearby GrC. The ubiquity of boutons throughout the axonal arbor is important in
596 light of potential alterative computations that could distribute inhibition to subsets of
597 neighboring GrCs to decorrelate or temporally sculpt responses. Such findings show that
598 cerebellar GoCs favor a blanket inhibitory process within the region.
599
600 The quantitative morphometry of reconstructed GoCs allowed us to evaluate how a population
601 of GoCs might contribute to spatial distribution of inhibition. Although partial reconstructions
602 of cerebellar GoCs have been published, they have most often followed labeling in brain slices
603 which necessarily exclude processes leaving or re-entering the slice (Kanichay and Silver,
604 2008; Vervaeke et al., 2010; Vervaeke et al., 2012; Szoboszlay et al., 2016; Valera et al., 2016).
605 Other published reconstructions have followed in vivo labeling but were incomplete (Simpson
606 et al., 2005; Barmack and Yakhnitsa, 2008). Nevertheless, these partial reconstructions support
607 the view advanced here that GoCs are characterized by dense axonal arbors but differ in the
608 extent and orientation of axonal fields (Simpson et al., 2005; Holtzman et al., 2006; Barmack
609 and Yakhnitsa, 2008). Recent work has identified microcircuitry differences between GoCs
610 with distinct molecular identities (Ankri et al., 2015). However, thus far it is unknown if such
611 connectivity and molecular identities extend to the morphology of GoCs. Future work should
612 relate molecular identity to morphological characteristics to clarify distinct functional roles for
613 GoC subtypes (Simat et al., 2007; Anrki et al., 2015; Eyre and Nusser, 2016).
614
615 The comprehensive reconstructions performed here offer insight into a GoC structural motif,
616 where boutons from individual cells remain tightly clustered even though the overall density of
617 boutons falls off with distance from the soma – that is, their nearest neighbor distances remain
618 constant, while the number of close neighbors drops off with distance from the soma.
619 Comparisons of the density of GlyT2-positive GoC boutons, which reflect upwards of 85% of
620 total GoC bouton population, with those of individual cells suggest that within 50 μm of a GoC
621 soma, a single GoC dominates the inhibitory axonal population. That dominance shifts as a
622 function of the distance from GoC somata: The distributions of the fraction of the GlyT2 GFP
623 labeled bouton density accounted for by an individual GoC (Fig 3E), indicate that a common
624 degree of overlap is around 5 GoC axons, since the distributions peak near 0.2, in line with

JNeurosci Accepted Manuscript

625 physiological estimates (Rossi and Hamann, 1998). The broadness of the distributions, however,
626 reveals that the number of overlapping GoCs can vary considerably – between 2 and 20 at
627 extremes. These differences are likely to produce a large variety of inhibitory environments
628 within a population of GrCs and may contribute to diversifying GrC responses to mossy fiber
629 input. Accounting for unlabeled GoC boutons does not alter these estimates substantially. Based
630 on estimates of glomerular density (Palkovits et al., 1971; Billings et al., 2014), our
631 measurements would suggest that, on average, an individual GoC makes between 0.5 and 1.5
632 boutons per glomerulus within its axonal field.
633
634 The conclusions drawn from the reconstruction data indicate that the GoC is in a position to
635 'globally' inhibit GrCs within range of its axonal arbors, as seen in thresholding motifs (Marr,
636 1969; Albus, 1971). However, examination of GrCs that were excited by optogenetic activation
637 of MF input revealed surprisingly sparse fast phasic inhibition, even when MF inputs were
638 dense (Fig.4). This seeming inconsistency was resolved by analyzing GrCs for spillover-like
639 slow inhibitory currents. This form of inhibition, which differs in kinetics and amplitude from
640 direct phasic inhibition, was always observed in GrCs activated by MFs. Slow spill-over
641 mediated IPSCs have been extensively studied in GrCs (Rossi and Hamann, 1998; Mitchell and
642 Silver, 2000; Rossi et al., 2003; Duguid et al., 2012; Duguid et al., 2015) and shown to
643 dominate inhibitory processing in GrCs. The difference in likelihood of fast phasic and slow
644 spillover currents, coupled with the extremely high density of GoC boutons suggested that fast
645 phasic inhibitory events occur probabilistically due to the chance spatial proximity of GrCs
646 dendrites relative to GoC axonal boutons. This view may be consistent with the observation that
647 'tonic inhibition' is present in the GCL: Tonic inhibition, which lacks resolvable inhibitory
648 current temporal modulation, may be at the end of a continuum of inhibitory current kinetics,
649 where the distance from GoC glomerular synapses to GrC dendrite postsynaptic sites dictates
650 kinetics.
651
652 Nevertheless, the striking differences between these IPSCs prompted further investigation into
653 the relative physiological roles of these forms of inhibition. Previous dynamic clamp studies
654 have shown that slow inhibition strongly inhibits GrCs (Crowley et al., 2009; Solinas et al.,
655 2010; Duguid et al., 2015; Kalmbach et al., 2011; Duguid et al., 2015)). We extended these

JNeurosci Accepted Manuscript

656 studies by combining physiological levels of inhibition through a dynamic clamp with
657 optogenetic activation of pontine MFs, offset in time from EPSPs. As expected, slow
658 spillover-like conductances, offset in time relative to opto-EPSPs reduced GrC responses to
659 both moderate frequency EPSPs and faster dynamically clamped EPSP trains.
660
661 Recent work has shown that mossy fiber mediated feedforward inhibition through GoCs is not
662 solely responsible for modulating GrC excitability and response timing. For instance, other
663 sources of drive to GoCs have recently been described, including from climbing fibers and
664 serotonin inputs (Fleming and Hull, 2018; Nietz et al., 2017). Moreover, physiological diversity
665 of mossy fiber drive to GrCs can modulate GrC response timing (Chabrol et al., 2015) – another
666 prominent role ascribed to GoC FFI. In addition, the duration and mixture of mossy fibers
667 activated can engage nonlinear recruitment patterns (Hernandez et al., 2018). Thus, future
668 studies should examine ways in which GoCs are recruited either independent of mossy fibers or
669 selectively by particular subpopulations.
670
671 Another source of complexity in relating MF activity to recruitment of feedforward inhibition is
672 the fact that EPSP-spike coupling in GoCs is heavily temporally filtered (Vervaeke et al., 2010;
673 Kanichay and Silver, 2008). Our study corroborated reports from several groups finding that
674 GoCs do not reliably follow increasing MF stimulation rates with high fidelity. Because our
675 study involved optogenetic recruitment of MFs labeled with a fluorophore, we could relate GoC
676 activation in our physiology recordings to the density and distribution of MFs activated by light.
677 We uncovered a linear relationship between active MF density and EPSC amplitudes in GoCs
678 elicited by light stimulation, indicative of convergence onto GoCs (Hernandez et al., 2018).
679 Furthermore, MF density related to the firing response elicited at a fixed stimulus rate. In
680 contrast to highly filtered EPSP-GoC firing rate relationships seen across the population and
681 with electrical stimulation, firing rates of GoCs that received the strongest EPSCs from
682 optogenetic stimuli (i.e. those with the highest density of MFs) linearly increased with
683 stimulation rates. These findings relate the density of MF activity to the recruitment of GoCs in
684 a rate-dependent manner, and suggest inhibitory mechanisms within the GCL maintain a large
685 dynamic range by integrating across both mossy fiber firing rate and density.

686 In conclusion this study relates GoC morphology and unique synaptic physiology onto GrCs to
687 local circuit computations that function to sparsen GrC activity relative to MF inputs by
688 reducing excitability. Our data reveal a strikingly dense inhibitory field of local GoCs,
689 analogous to the widefield inhibitory interneurons in insect mushroom bodies (Papadopoulou et
690 al., 2011) and show that individual GoCs integrate many MF inputs to regulate their output,
691 driving activity that scales with input. Thus, the GoC occupies a key multimodal integrative
692 niche within the layer that, compared to the extremely limited extent of the GrC dendrite,
693 allows for a broader integration of multimodal signals to regulate GrC population activity.

694

695 **References**

696 Albus JS (1971) A theory of cerebellar function. Mathematical Biosciences 10:25-61.
697 Ankri L, Yarom Y, Uusisaari MY (2014) Slice it hot: acute adult brain slicing in physiological
698 temperature. J Vis Exp. 92:e52068
699 Ankri L, Husson Z, Pietrajtis K, Proville R, Lena C, Yarom Y, Dieudonne S, Uusisaari MY
700 (2015) A novel inhibitory nucleo-cortical circuit controls cerebellar Golgi cell activity.
701 Elife 4.
702 Barmack NH, Yakhnitsa V (2008) Functions of interneurons in mouse cerebellum. J Neurosci
703 28:1140-1152.
704 Billings G, Piasini E, Lorincz A, Nusser Z, Silver RA (2014) Network structure within the
705 cerebellar input layer enables lossless sparse encoding. Neuron 83:960-974.
706 Brickley SG, Cull-Candy SG, Farrant M (1996) Development of a tonic form of synaptic
707 inhibition in rat cerebellar granule cells resulting from persistent activation of GABAA
708 receptors. J Physiol 497 (Pt 3):753-759.
709 Cayco-Gajic NA, Clopath C, Silver RA (2017) Sparse synaptic connectivity is required for
710 decorrelation and pattern separation in feedforward networks. Nat Commun 8:1116.
711 Cesana E, Pietrajtis K, Bidoret C, Isope P, D'Angelo E, Dieudonne S, Forti L (2013) Granule
712 cell ascending axon excitatory synapses onto Golgi cells implement a potent feedback
713 circuit in the cerebellar granular layer. J Neurosci 33:12430-12446.
714 Chabrol FP, Arenz A, Wiechert MT, Margrie TW, DiGregorio DA (2015) Synaptic diversity
715 enables temporal coding of coincident multisensory inputs in single neurons. Nat
716 Neurosci 18:718-727.
717 Crowley JJ, Fioravante D, Regehr WG (2009) Dynamics of fast and slow inhibition from
718 cerebellar golgi cells allow flexible control of synaptic integration. Neuron 63:843-853.

JNeurosci Accepted Manuscript

JNeurosci Accepted Manuscript

719 D'Angelo E, De Zeeuw CI (2009) Timing and plasticity in the cerebellum: focus on the granular
720 layer. Trends Neurosci 32:30-40.
721 D'Angelo E, Solinas S, Mapelli J, Gandolfi D, Mapelli L, Prestori F (2013) The cerebellar
722 Golgi cell and spatiotemporal organization of granular layer activity. Front Neural
723 Circuits 7:93.
724 Desai NS, Gray R, Johnston D (2017) A Dynamic Clamp on Every Rig. eNeuro 4.
725 Duguid I, Branco T, London M, Chadderton P, Hausser M (2012) Tonic inhibition enhances
726 fidelity of sensory information transmission in the cerebellar cortex. J Neurosci
727 32:11132-11143.
728 Duguid I, Branco T, Chadderton P, Arlt C, Powell K, Hausser M (2015) Control of cerebellar
729 granule cell output by sensory-evoked Golgi cell inhibition. Proc Natl Acad Sci U S A
730 112:13099-13104.
731 Eccles JC, Ito M, Szentagothai J (1967) The Cerebellum as a Neuronal Mechine. Berlin:
732 Springer-Verlag.
733 Eyre MD, Nusser Z (2016) Only a minority of the inhibitory inputs to cerebellar Golgi cells
734 originates from local GABAergic cells. eNeuro 3(2). doi: 10.1523
735 Farrant M, Nusser Z (2005) Variations on an inhibitory theme: phasic and tonic activation of
736 GABA(A) receptors. Nat Rev Neurosci 6:215-229.
737 Fleming E, Hull C (2018) Serotonin regulates the dynamics of cerebellar granule cell activity
738 by modulating tonic inhibition. J Neurophysiol doi10.1152
739 Gao Z, Proietti-Onori M, Lin Z, Ten Brinke MM, Boele HJ, Potters JW, Ruigrok TJ, Hoebeek
740 FE, De Zeeuw CI (2016) Excitatory Cerebellar Nucleocortical Circuit Provides Internal
741 Amplification during Associative Conditioning. Neuron 89:645-657.
742 Gilmer JI, Person AL (2017) Morphological Constraints on Cerebellar Granule Cell
743 Combinatorial Diversity. J Neurosci 37:12153-12166.
744 Hamann M, Rossi DJ, Attwell D (2002) Tonic and spillover inhibition of granule cells control
745 information flow through cerebellar cortex. Neuron 33:625-633.
746 Hernandez O, Pietrajtis K, Mathieu B, Dieudonné S (2018) Optogenetic stimulation of complex
747 spatio-temporal activity patterns by acousto-optic light steering probes cerebellar
748 granular layer integrative properties. Sci Rep 8, 13768
749 Holtzman T, Rajapaksa T, Mostofi A, Edgley SA (2006) Different responses of rat cerebellar
750 Purkinje cells and Golgi cells evoked by widespread convergent sensory inputs. J
751 Physiol 574:491-507.
752 Honda T, Ito M (2017) Development from Marr's theory of the cerebellum. In: Computational
753 theories and their implementation in the brain : the legacy of David Marr (Vaina LM and

JNeurosci Accepted Manuscript

754 Passingham RE, ed), First edition. Edition. Oxford: Oxford University Press.
755 Huang CC, Sugino K, Shima Y, Guo C, Bai S, Mensh BD, Nelson SB, Hantman AW (2013)
756 Convergence of pontine and proprioceptive streams onto multimodal cerebellar granule
757 cells. Elife 2:e00400.
758 Hull C, Regehr WG (2012) Identification of an inhibitory circuit that regulates cerebellar Golgi
759 cell activity. Neuron 73:149-158.
760 Ishikawa T, Shimuta M, Hausser M (2015) Multimodal sensory integration in single cerebellar
761 granule cells in vivo. Elife 4.
762 Jakab RL, Hamori J (1988) Quantitative morphology and synaptology of cerebellar glomeruli
763 in the rat. Anat Embryol (Berl) 179:81-88.
764 Kalmbach BE, Voicu H, Ohyama T, Mauk MD (2011) A subtraction mechanism of temporal
765 coding in cerebellar cortex. J Neurosci 31:2025-2034.
766 Kanichay RT, Silver RA (2008) Synaptic and cellular properties of the feedforward inhibitory
767 circuit within the input layer of the cerebellar cortex. J Neurosci 28:8955-8967.
768 Mapelli L, Rossi P, Nieus T, D'Angelo E (2009) Tonic activation of GABAB receptors reduces
769 release probability at inhibitory connections in the cerebellar glomerulus. J
770 Neurophysiol 101:3089-3099.
771 Marr D (1969) A theory of cerebellar cortex. J Physiol 202:437-470.
772 Medina JF, Garcia KS, Nores WL, Taylor NM, Mauk MD (2000) Timing mechanisms in the
773 cerebellum: testing predictions of a large-scale computer simulation. J Neurosci
774 20:5516-5525.
775 Mitchell SJ, Silver RA (2000) Glutamate spillover suppresses inhibition by activating
776 presynaptic mGluRs. Nature 404:498-502.
777 Mitchell SJ, Silver RA (2003) Shunting inhibition modulates neuronal gain during synaptic
778 excitation. Neuron 38:433-445.
779 Nietz AK, Vaden JH, Coddington LT, Overstreet-Wadiche L, Wadiche JI (2017) Non-synaptic
780 signaling from cerebellar climbing fibers modulates Golgi cell activity. Elife pii:e29215
781 Nieus TR, Mapelli L, D'Angelo E (2014) Regulation of output spike patterns by phasic
782 inhibition in cerebellar granule cells. Front Cell Neurosci 8:246.
783 Palay SL, Chan-Palay V (1974) Cerebellar Cortex Cytology and Organication.
784 Palay SL, Chan-Palay V (1976) A guide to the synaptic analysis of the neuropil. Cold Spring
785 Harb Symp Quant Biol 40:1-16.
786 Palkovits M, Magyar P, Szentagothai J (1971) Quantitative histological analysis of the
787 cerebellar cortex in the cat. II. Cell numbers and densities in the granular layer. Brain
788 Res 32:15-30.

JNeurosci Accepted Manuscript

789 Papadopoulou M, Cassenaer S, Nowotny T, Laurent G (2011) Normalization for sparse
790 encoding of odors by a wide-field interneuron. Science 332:721-725.
791 Pellionisz A, Szentagothai J (1973) Dynamic single unit simulation of a realistic cerebellar
792 network model. Brain Res 49:83-99.
793 Person AL, Raman IM (2011) Purkinje neuron synchrony elicits time-locked spiking in the
794 cerebellar nuclei. Nature 481: 502-5.
795 Pouille F, Marin-Burgin A, Adesnik H, Atallah BV, Scanziani M (2009) Input normalization by
796 global feedforward inhibition expands cortical dynamic range. Nat Neurosci
797 12:1577-1585.
798 Rossi DJ, Hamann M (1998) Spillover-mediated transmission at inhibitory synapses promoted
799 by high affinity alpha6 subunit GABA(A) receptors and glomerular geometry. Neuron
800 20:783-795.
801 Rossi DJ, Hamann M, Attwell D (2003) Multiple modes of GABAergic inhibition of rat
802 cerebellar granule cells. J Physiol 548:97-110.
803 Rudolph S, Hull C, Regehr WG (2015) Active Dendrites and Differential Distribution of
804 Calcium Channels Enable Functional Compartmentalization of Golgi Cells. J Neurosci
805 35:15492-15504.
806 Saviane C, Silver RA (2006) Fast vesicle reloading and a large pool sustain high bandwidth
807 transmission at a central synapse. Nature 439:983-7.
808 Simat M, Parpan F, Fritschy JM (2007) Heterogeneity of glycinergic and gabaergic interneurons
809 in the granule cell layer of mouse cerebellum. J Comp Neurol 500:71-83.
810 Simpson JI, Hulscher HC, Sabel-Goedknegt E, Ruigrok TJ (2005) Between in and out: linking
811 morphology and physiology of cerebellar cortical interneurons. Prog Brain Res
812 148:329-340.
813 Solinas S, Nieus T, D'Angelo E (2010) A realistic large-scale model of the cerebellum granular
814 layer predicts circuit spatio-temporal filtering properties. Front Cell Neurosci 4:12.
815 Szoboszlay M, Lorincz A, Lanore F, Vervaeke K, Silver RA, Nusser Z (2016) Functional
816 Properties of Dendritic Gap Junctions in Cerebellar Golgi Cells. Neuron 90:1043-1056.
817 Valera AM, Binda F, Pawlowski SA, Dupont JL, Casella JF, Rothstein JD, Poulain B, Isope P
818 (2016) Stereotyped spatial patterns of functional synaptic connectivity in the cerebellar
819 cortex. Elife 5.
820 Vervaeke K, Lorincz A, Nusser Z, Silver RA (2012) Gap junctions compensate for sublinear
821 dendritic integration in an inhibitory network. Science 335:1624-1628.
822 Vervaeke K, Lorincz A, Gleeson P, Farinella M, Nusser Z, Silver RA (2010) Rapid
823 desynchronization of an electrically coupled interneuron network with sparse excitatory

JNeurosci Accepted Manuscript

824 synaptic input. Neuron 67:435-451.
825 Walcott EC, Higgins EA, Desai NS (2011) Synaptic and intrinsic balancing during postnatal
826 development in rat pups exposed to valproic acid in utero. J Neurosci 31: 13097-13109
827 Wall MJ, Usowicz MM (1997) Development of action potential-dependent and independent
828 spontaneous GABAA receptor-mediated currents in granule cells of postnatal rat
829 cerebellum. Eur J Neurosci 9:533-548.
830
831

JNeurosci Accepted Manuscript

832
833
834 **Figure 1. Sparse viral label and comprehensive reconstruction of cerebellar GoCs**
835 **A**, Schematic of sparse viral labeling technique where low titre AAV8-hSyn1-mCherry-Cre 10^2
836 and high titre AAV2-CAG-FLEX-EGFP 10^{12} were coinjected to cerebellar cortex. Bottom,
837 representative example of GoC axonal boutons. **B**, Example of a sparsely labeled GoC. Scale:
838 20 μm. **C**, Comprehensive, 3D reconstruction of GoC displayed in 2D. Red, axon; Cyan: basal
839 dendrite; Yellow: apical dendrite, Beige, soma. Left: overview of the single GoC. Middle: axon
840 processes in GCL. Right: apical dendrites and basal dendrites. Scale: 50 μm. **D**, Total length of
841 each process type. **E**, Convex hull volume of each process type. **F**, Maps of axonal boutons
842 from two representative sparsely labeled GoCs. Black dots indicate the location of each bouton
843 and green circle indicates soma.
844

JNeurosci Accepted Manuscript

845

846 **Figure 2. Clustered boutons revealed with high resolution mapping**

847 **A**, Bouton map of GoC with distance to the nearest bouton represented by color. **B**, Probability
848 histogram of nearest bouton distances in five GoCs (gray) and mean of five cells (blue, shaded
849 area, sd). Bin width: 0.1 µm. **C**, Summary of nearest boutons as a function of distance from
850 soma. Lines indicate linear regressions plotted for each neuron. **D**, Bouton map of the same
851 GoC shown in *A* with the number of boutons within 10 µm radius from each individual bouton
852 represented by color. **E**, Number of boutons within 10 µm radius from each bouton as a
853 function of distance from the soma. Lines indicate linear regressions plotted for each neuron.
854

855 **Figure 3. Contribution of single GoCs to population distribution**

856 **A**, GlyT2-eGFP expressing processes in mouse GCL. Scale: 10 µm. **B**, Probability histograms
857 of nearest bouton distances for single GoCs (black) and the population of GoCs labeled with
858 GlyT2-GFP (red). Bin width: 0.25 µm. **C**, Probability histograms of average distances to the
859 closest 10 boutons from each bouton for single GoCs (black) and a population of GoCs labeled
860 with GlyT2-GFP (red). Bin width: 0.25 µm. **D**, Ratio of single GoC bouton density to the
861 population-level bouton density as a function of distance from GoC soma. The mean GlyT2
862 bouton density within a 25 µm radius sphere was compared to the number of boutons within a
863 25 µm radius sphere for each bouton in the single GoCs. Lines indicate linear regressions
864 plotted for each neuron. **E**, Probability histogram plotting the ratio of the total GlyT2 bouton
865 density accounted for by one GoC. Bin width: 0.05.
866

867 **Figure 4. GrC responses to optogenetic activation of identified MF populations**

868 **A**, Schematic diagram of recording configuration. ChR2-expressing NC or pontine MFs were
869 optogenetically stimulated during GrC recordings. **B and C**, Overlaid EPSCs or IPSCs evoked
870 by 2 ms optogenetic stimulation of NC MFs at -70 or 0 mV holding.
871 **D**, Latency of EPSCs and fast phasic IPSCs ($p < 0.001$; unpaired t-test, gray bar = mean). **E**,
872 Jitter of timing of EPSCs and fast phasic IPSCs was significantly different ($p < 0.001$, unpaired
873 t-test; bar = mean). **F and G**, Representative traces of responses to light stimulation following
874 NC MF stimulation at -70 mV (solid lines) and 0 mV (dashed lines). **H**, Example of slow
875 outward current evoked after optogenetic stimulation of NC pathway at 20 Hz, Vhold = 0 mV. **I,**
876 Summary of fast phasic current amplitudes recorded at -70 or 0 mV. **J,** Summary of charge
877 transfer during slow outward currents evoked by NC MF stimulation. **K-M,** Same as F-G but
878 for pontine MF stimulation. **N,** Example of slow outward current evoked after optogenetic
879 stimulation of pontine MFs at 20 Hz, Vhold = 0 mV. **O,** Same as I but for pontine MF

JNeurosci Accepted Manuscript

880 stimulation. **P,** Same as J but for pontine MF stimulation.

881

882 **Figure 5. Predominant role for slow feedforward inhibition in regulating GrC synaptic**
883 **responses at moderate excitation frequency. A,** *Left*, Schematic of recording configuration
884 where dynamic clamp and optogenetic MF stimulation were combined to examine the role of
885 feedforward inhibition (A). *Right*, Representative traces showing GrC responses to 20 Hz
886 optogenetic stimulation of pontine MFs without (top trace) and with (lower trace) dynamic
887 clamp physiological fast phasic IPSGs (bottom). Below, the same conventions describe
888 experiments using dynamic clamp to mimic 100 Hz excitation and 60 Hz inhibition. **B**, Black,
889 summary of MF opto-evoked firing rate changes with and without small fast phasic IPSGs. Red,
890 same but for dynamic clamp EPSG+IPSGs. **C-D**, Same as A-B except with large fast phasic
891 IPSGs. **E-F** Same as A-B except with small, slow phasic IPSGs. Bottom, representative trace
892 from GrC in response to 50 Hz light train illustrating similarity to injected conductance. **G-H**,
893 Same as A-B except with large, slow phasic IPSGs. Significant changes in firing rate were
894 observed in 7/8 GrCs ($p<0.05$, paired t-tests).

895

896 **Figure 6. GoC recruitment follows MF population activity levels. A**, Schematic diagram of
897 recording configuration. ChR2-expressing NC or Pontine MFs were stimulated during GoC
898 recordings. **B**, Biocytin filled GoCs (cyan) recovered after recordings show proximity of
899 RFP-expressing MFs. Scale: 50 μm. Right, Putative synaptic contacts (arrows) or absence of
900 contacts between recorded GoC and MF, associated with physiological traces in C and D shown
901 in transparency rendering mode. **C**, Representative examples of GoC evoked firing in response
902 to optogenetic stimulation of pontine MFs at 40 Hz. Responses varied between cells
903 (top-bottom). **D**, Representative traces showing diversity of evoked EPSCs following
904 optogenetic stimulation of pontine MFs at 40 Hz. Vhold = -70 mV. Traces in D are matched
905 with current clamp responses in C. **E and F**, Relationship of GoC firing rate change to
906 stimulation rate. Non-significant relationships are shown in E, Significant relationships are
907 shown in F. **G,** Probability distribution of initial EPSC amplitudes measured in GoCs showing
908 significant (black; data from F) or non-significant (red; data from E) input-output relationships.
909 **H,** Relationship of EPSC amplitude to ChR2-expressing MF density. (R^2= 0.44, p = 0.001,
910 F=14.3, df=18, n=20). **I,** Relationship of GoC firing rate change to 40 Hz stimulation as a
911 function of ChR2-expressing MF density. (R^2 = 0.23; p=0.04; F= 5.0; df= 16; n= 18). **J**,
912 Multi-EPSC-peak probability plotted as a function of initial EPSC amplitude. (R^2=0.41,
913 $p<0.0001$, F=27.9, DF=40, n=42).

914

JNeurosci Accepted Manuscript

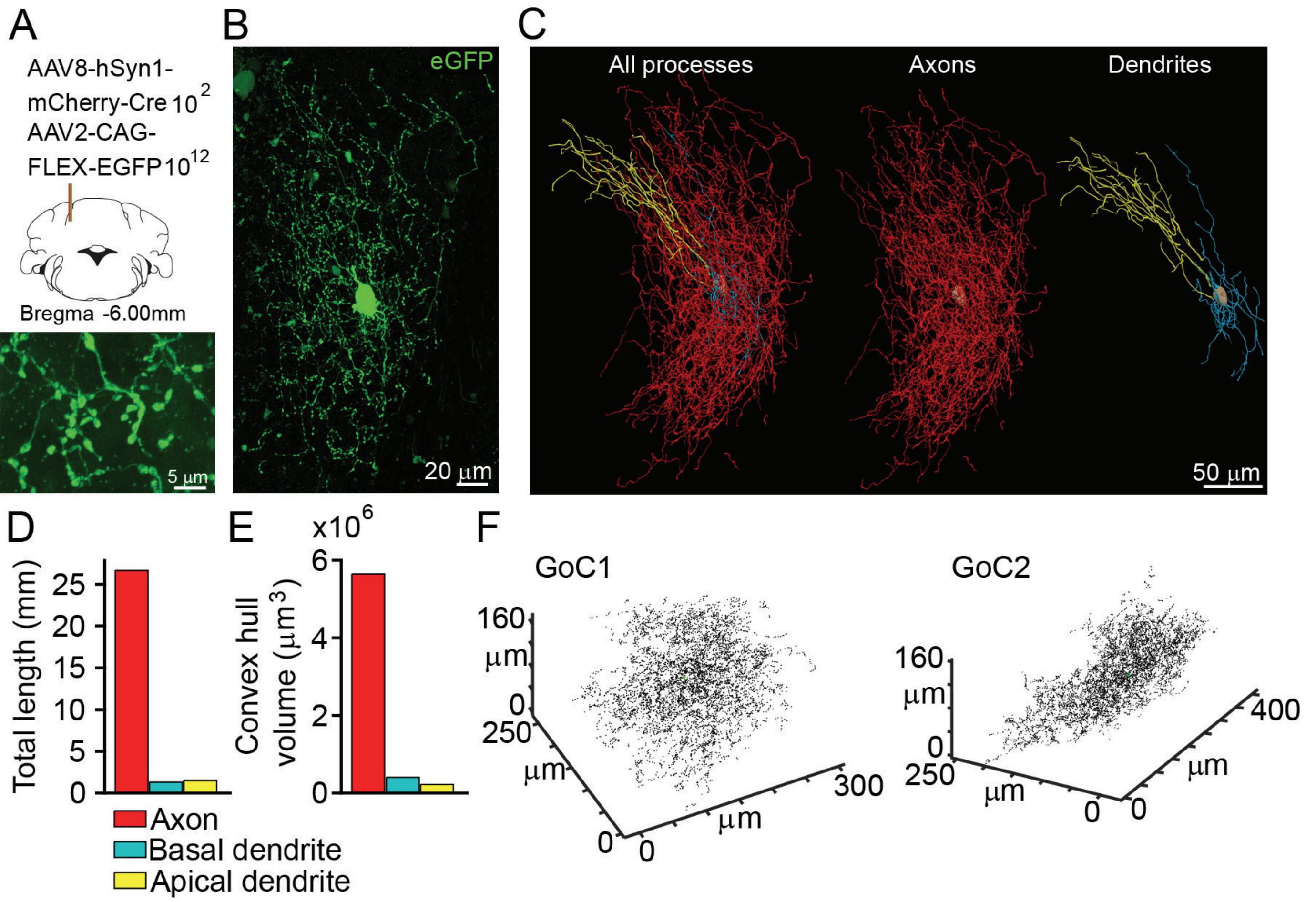

JNeurosci Accepted Manuscript

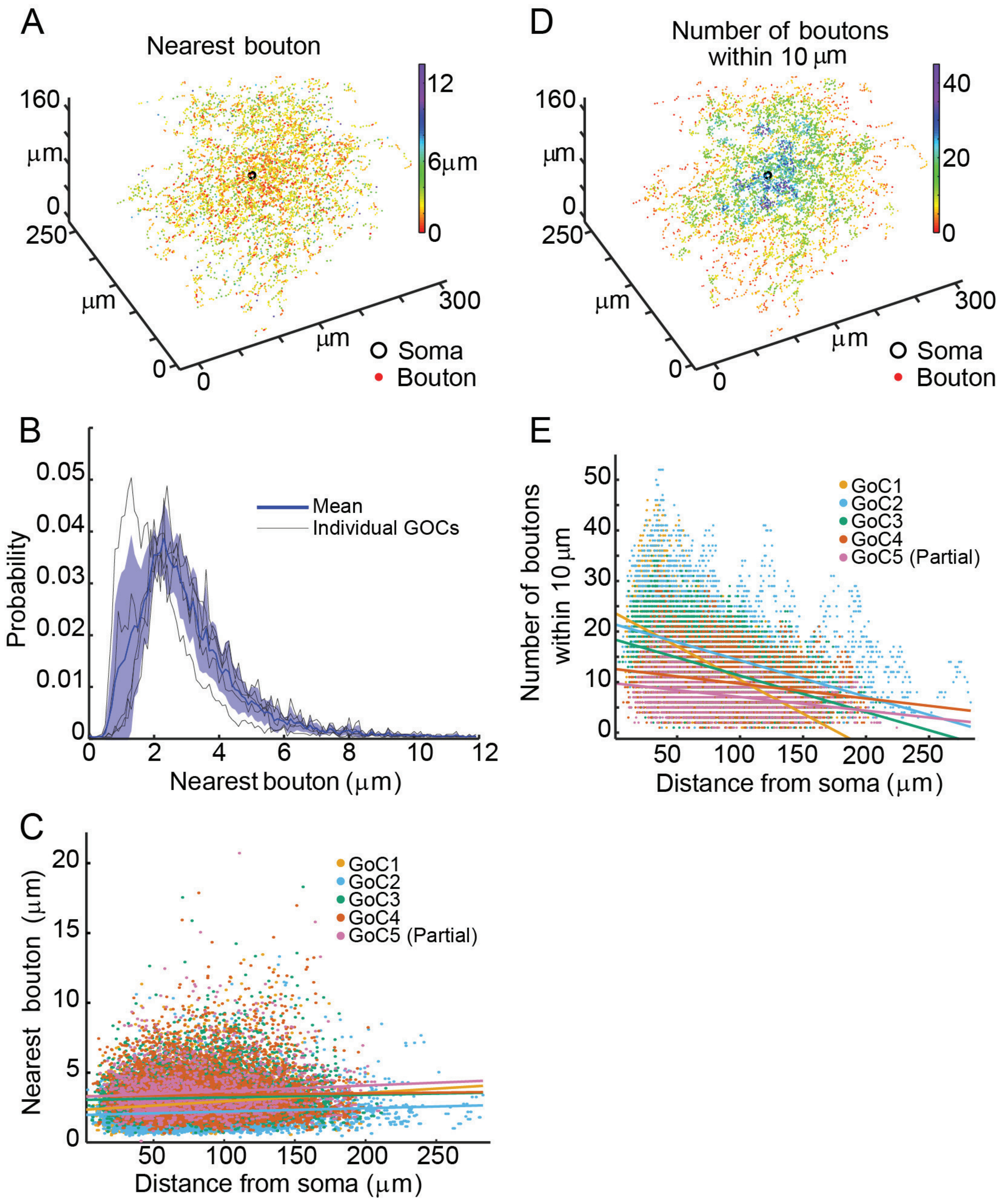

JNeurosci Accepted Manuscript

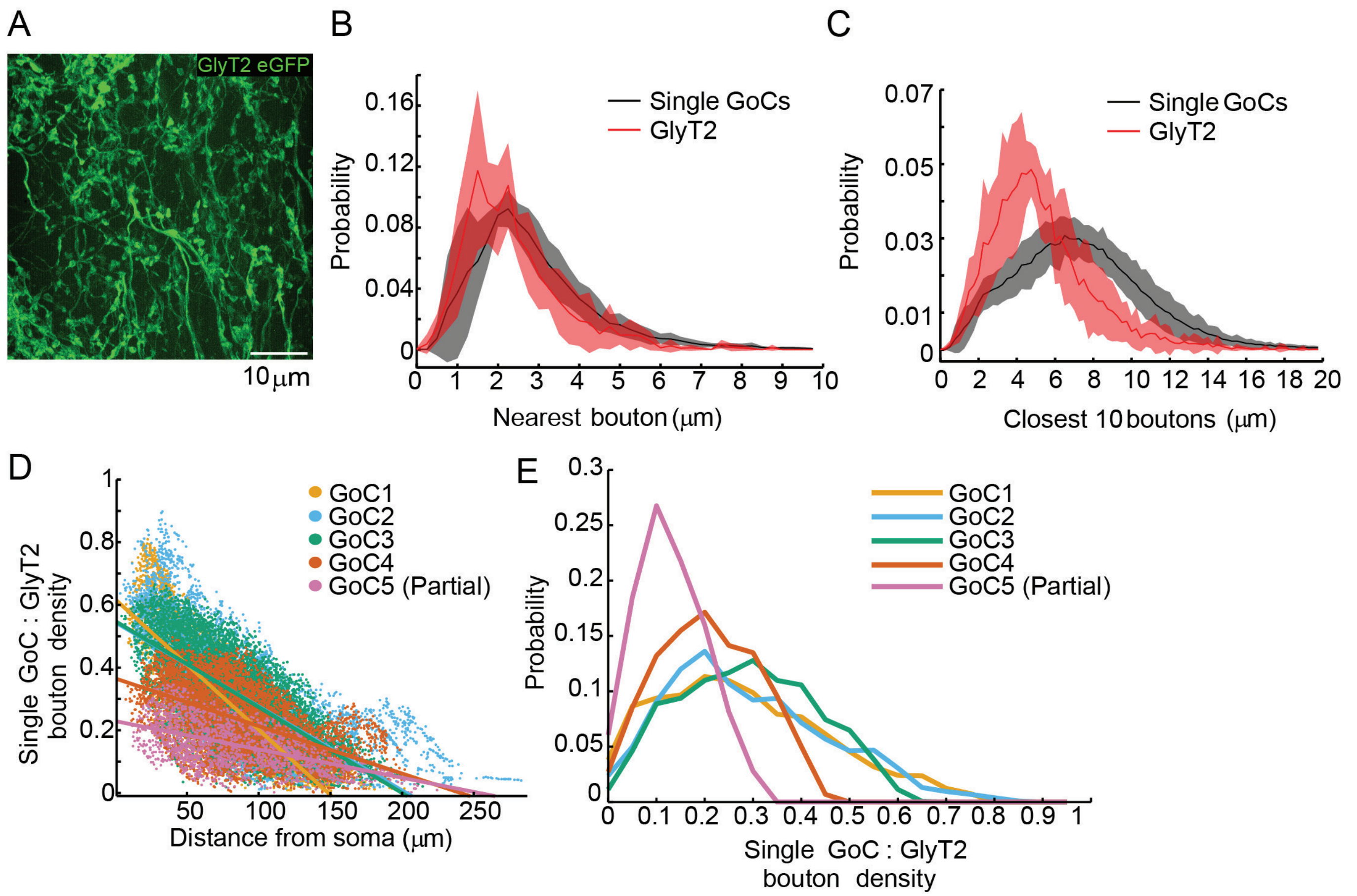

JNeurosci Accepted Manuscript

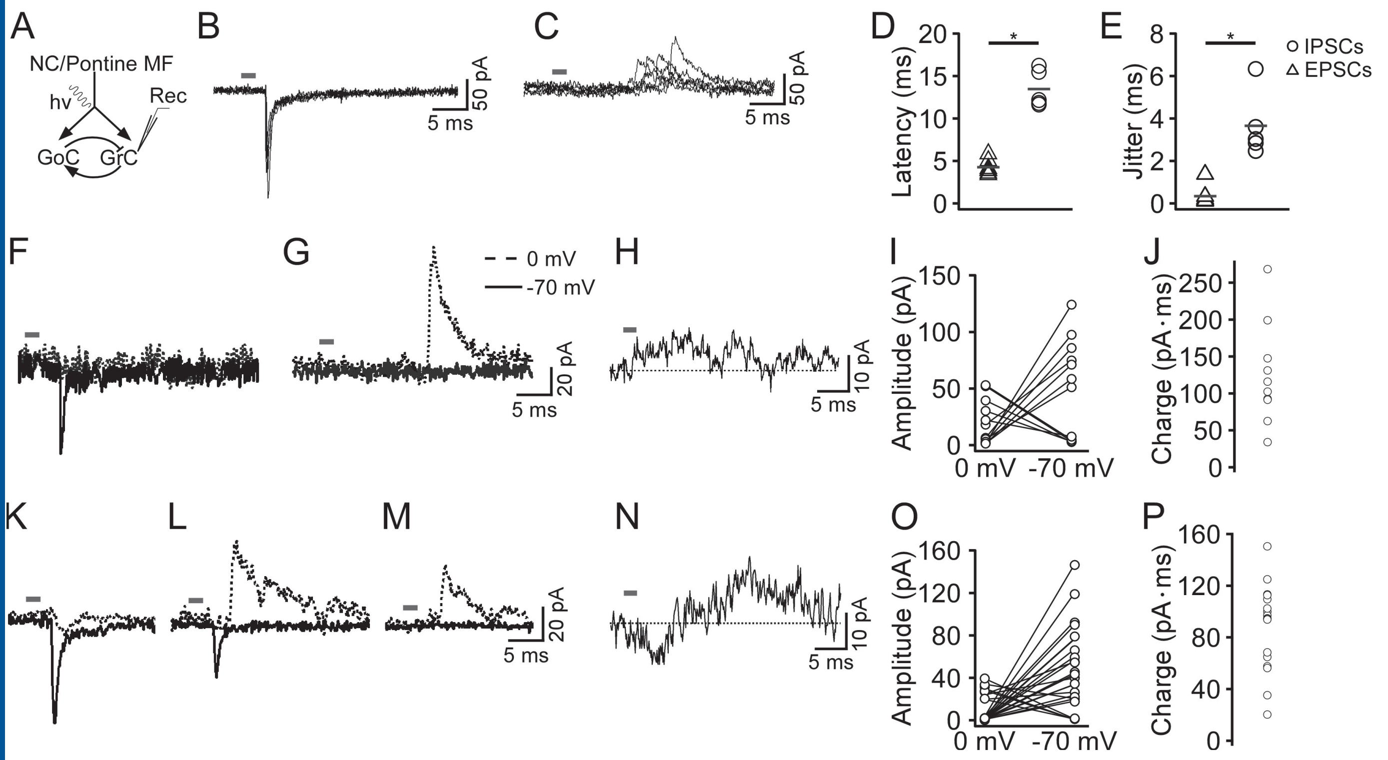

JNeurosci Accepted Manuscript

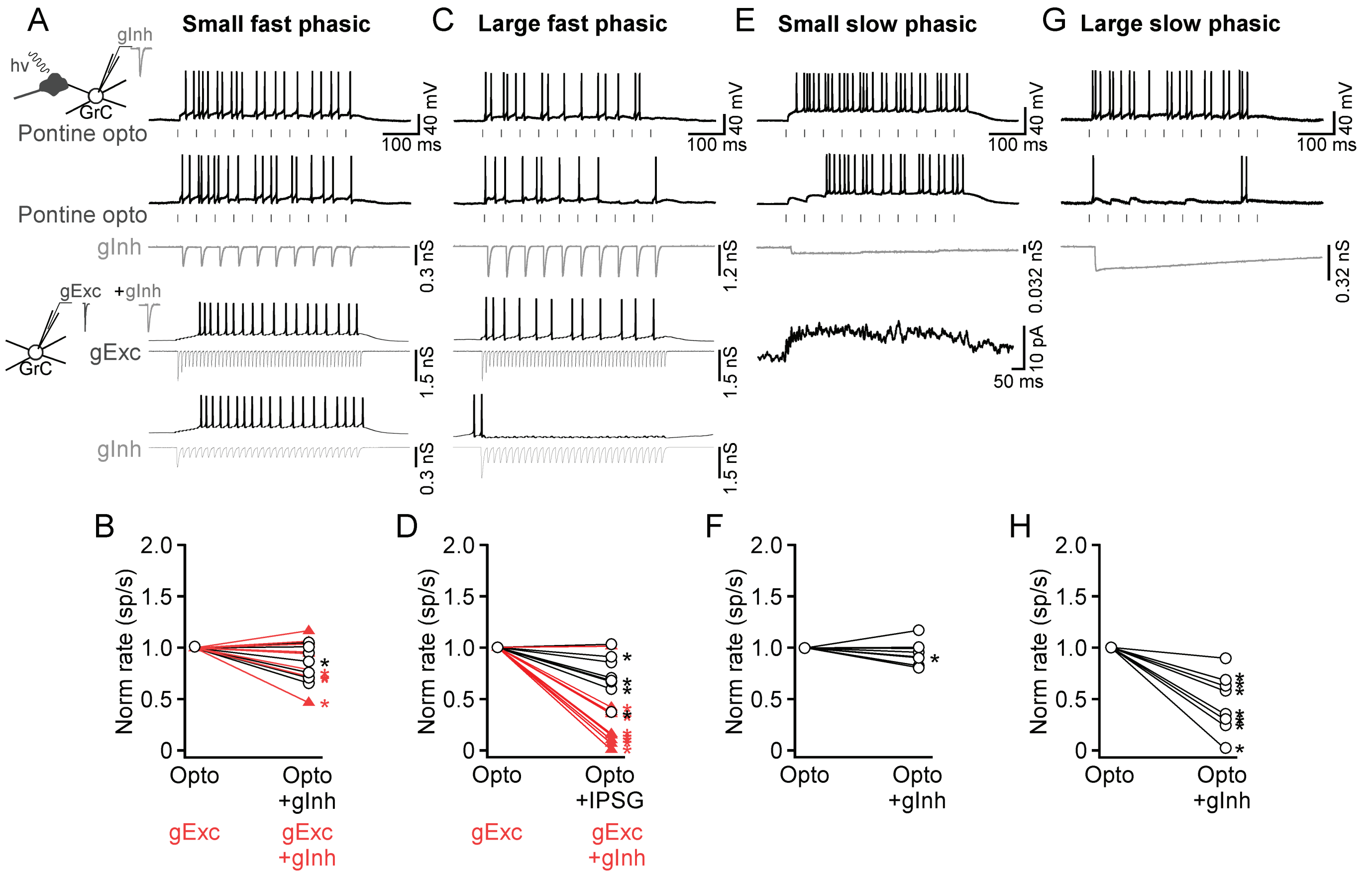

JNeurosci Accepted Manuscript